Covalent-Organic-Framework-Based Li–CO$_2$ Batteries

Xing Li, Hui Wang, Zhongxin Chen, Hai-Sen Xu, Wei Yu, Cuibo Liu, Xiaowei Wang, Kun Zhang, Keyu Xie,* and Kian Ping Loh*

Covalent organic frameworks (COFs) are an emerging class of porous crystalline materials constructed from designer molecular building blocks that are linked and extended periodically via covalent bonds. Their high stability, open channels, and ease of functionalization suggest that they can function as a useful cathode material in reversible lithium batteries. Here, a COF constructed from hydrazone/hydrazide-containing molecular units, which shows good CO$_2$ sequestration properties, is reported. The COF is hybridized to Ru-nanoparticle-coated carbon nanotubes, and the composite is found to function as highly efficient cathode in a Li–CO$_2$ battery. The robust 1D channels in the COF serve as CO$_2^-$ and lithium-ion-diffusion channels and improve the kinetics of electrochemical reactions. The COF-based Li–CO$_2$ battery exhibits an ultrahigh capacity of 27 348 mAh g^{-1} at a current density of 200 mA g^{-1}, and a low cut-off overpotential of 1.24 V within a limiting capacity of 1000 mAh g^{-1}. The rate performance of the battery is improved considerably with the use of the COF at the cathode, where the battery shows a slow decay of discharge voltage from a current density of 0.1 to 4 A g^{-1}. The COF-based battery runs for 200 cycles when discharged/charged at a high current density of 1 A g^{-1}.

Covalent organic frameworks (COFs) are molecular Legos where small-molecular building units are covalently connected in a periodic network.[1–4] The high stability endowed by the strong covalent linkage and the ease of encoding functionalities render COFs potentially useful as light-emitting,[5,6] catalytic,[7–10] and energy storage[11–14] materials. COF can be competitive especially under environment where metal–organic frameworks (MOFs) are unstable, and where polymeric materials undergo undesirable phase change. Today, the requirement for a low carbon footprint is almost universal in developed countries; thus, there is a need to sequester and utilize CO$_2$. MOFs and COFs have been

Dr. X. Li, Dr. Z. Chen, Dr. H.-S. Xu, W. Yu, C. Liu, X. Wang, K. Zhang, Prof. K. Xie, Prof. K. P. Loh
Department of Chemistry
National University of Singapore
3 Science Drive 3, Singapore 117543, Singapore
E-mail: kyxie@nwpu.edu.cn; chmlohkp@nus.edu.sg
H. Wang, K. Zhang, Prof. K. Xie
State Key Laboratory of Solidification Processing
Center for Nano Energy Materials
Northwestern Polytechnical University and Shaanxi Joint Laboratory of Graphene (NPU)
Xi'an 710072, P. R. China

considered as alternatives to the amine gas treatment process for CO$_2$ capture due to its thermal stability, porosities, and functional groups.[15,16] The ordered porosity in COFs provide tailor-made 1D channels for gas storage/separation[17–22] as well as ion conduction;[23–30] thus, it is timely to explore the use of COFs in metal–gas-type batteries. Li–CO$_2$ batteries[31–38] are based on futuristic technology that can directly utilize CO$_2$ gas for energy storage, showing great value not only in the sequestration of CO$_2$, but also utilizing it for energy storage under extreme conditions, e.g., terraforming; 95.32% of the atmosphere of Mars is CO$_2$.[39] An ideal CO$_2$ cathode should fulfill the following requirements: 1) good CO$_2$ capture ability; 2) low overpotential for battery charging and discharging; 3) high reversibility for long-term cycling; and 4) good rate performance for rapid discharging/charging. Currently, researchers are actively searching for CO$_2$ electrode materials that can meet the above criteria. Conventional cathodes, usually made of conductive carbon materials coated with metal catalyst,[40–42] suffer from low energy capacity caused by poor CO$_2$ capture, short cycle life due to irreversible discharge product's (Li$_2$CO$_3$/C) accumulation, and poor rate performance. The rate performance of Li–CO$_2$ battery is currently far from ideal due to sluggish kinetics of discharging/charging reactions and the lack of a solution for an electrolyte which can be a fast diffusion medium not only for Li ions but also for CO$_2$.

Properly designed COFs with atomically precise open channels and skeletons provide an ideal platform to investigate ion and gas transport relevant to CO$_2$-cathode materials. When such COFs are mixed with conventional cathode materials (**Figure 1**), they can potentially play the role of a CO$_2$ collector during the discharging process to improve the energy capacity, and also during charging process to facilitate Li$_2$CO$_3$ decomposition. Moreover, COFs can serve as diffusion layers for both Li ion and CO$_2$ gas, thereby enhancing the rate performance for battery charge/discharge. Here, we report an efficient COF-based cathode constructed from a hybrid of hydrazone COF and Ru nanoparticle-decorated carbon nanotube (Ru@CNT). The COF-based cathode shows a low overpotential of 1.24 V for Li–CO$_2$ batteries and the battery exhibits an ultrahigh capacity of 27 348 mAh g^{-1} at a current density of 200 mA g^{-1}, which is almost three times of that of battery using Ru@CNT cathode. Most importantly, our COF-based battery displays excellent rate
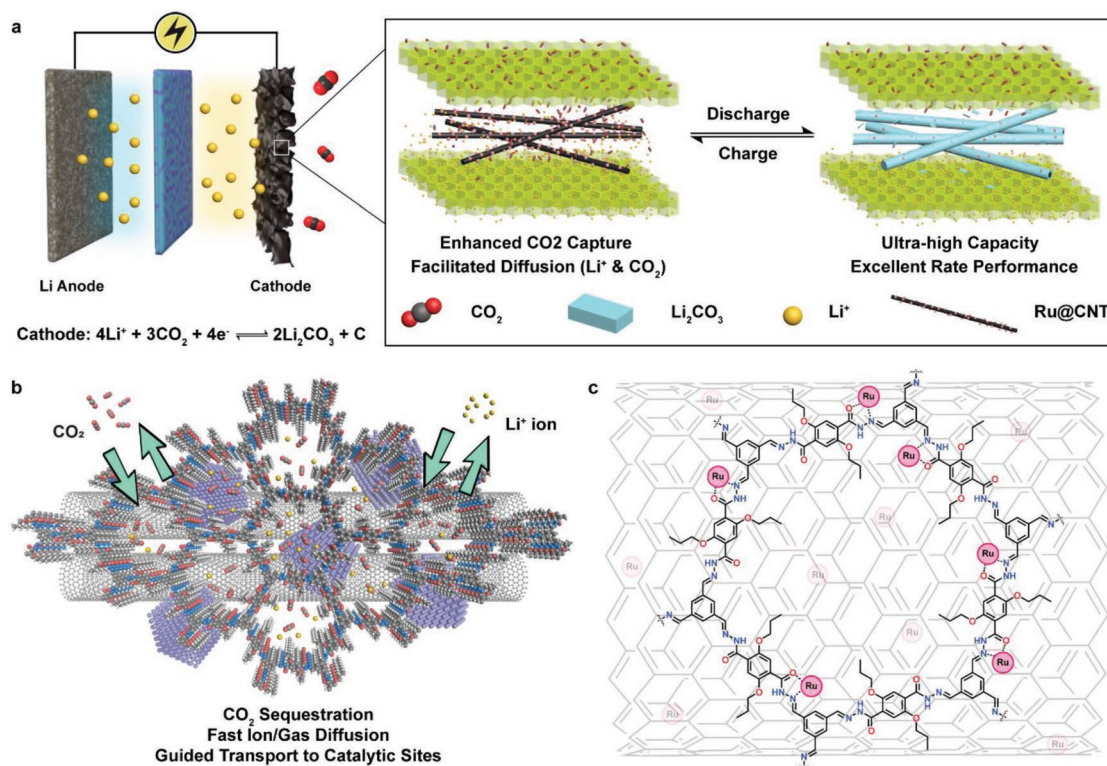
Figure 1. a) Schematic illustration of COF working as the CO_2 collector and the gas-ion diffusion channels for Li–CO_2 battery cathode. b,c) Synthesis of highly crystalline Tf–DHzOPr COF interfaced with Ru@CNT via hydrazide–metal coordination.

performance with a low discharging voltage loss up to 4000 mA g^{-1}, which is the best performance among all reported Li–CO_2 batteries to date. The good kinetics allow our COF-based battery to run 200 cycles stably with no obvious decay of discharge/charge voltage under a high current density of 1000 mA g^{-1}.

The working mechanism of Li–CO_2 batteries has been discussed extensively in previous research.[34–36] During the discharging process of the battery, the CO_2 captured is converted to electrochemically inert Li_2CO_3 and carbon. This process is typically irreversible; thus, there exists a large voltage gap between discharge and charge processes, leading to poor rate performance and short cycle life. Conventional approaches to mitigate this problem rely on catalytic nanoparticles that are immobilized on a carbon material (e.g., carbon nanotubes) to catalyze the decomposition of Li_2CO_3 and carbon reversibly back to CO_2.[40,41,43,44] However, the poor kinetics of Li–CO_2 batteries such as the sluggish diffusion of CO_2 and Li ions deserve attention. The dissolution of CO_2 is usually poor in the electrolyte; thus, the battery discharging/charging current is limited due to low efficiency of CO_2 diffusion. Furthermore, the lack of interconnected ion transport and gas diffusion channels in general electrode material results in sluggish kinetics. Herein, our strategy is to design well-tailored open channels in COF to serve as a CO_2 collector and both ion-transport and gas-diffusion channels when interfaced to Ru nanoparticles supported on CNT (Ru@CNT), whereby Ru is a common catalyst responsible for CO_2 reduction and Li_2CO_3/C decomposition.[40] The working principle of the COF-based Li–CO_2 battery is illustrated in Figure 1. The presence of requisite functional groups

on pore edges allows COF to coordinate to Ru atoms on CNT, and its 1D channel facilitates the transport of both CO_2 gas and Li ions, thus allowing the Li_2CO_3/C to form fast and decompose fast at the interface of COF and Ru@CNT.

The Ru@CNT was prepared through reduction of $RuCl_3$ in a suspension of CNT in ethylene glycol.[40] Confirmed by dark-field scanning transmission electron microscopy (STEM), the Ru nanoparticles were successfully attached to CNTs (**Figure 2**b). Inductively coupled plasma–optical emission spectrometry (ICP-OES) revealed that the Ru content in Ru@CNT was 15.9 wt%. X-ray photoelectron spectroscopy (XPS) study confirmed that the Ru(III) was successfully reduced to Ru(0) on the CNT, with the characteristic core level peaks at ≈462.5 eV for Ru $3p_{3/2}$ and ≈484.9 eV for Ru $3p_{1/2}$[45] (Figure S1, Supporting Information); this is important because metallic Ru is the active catalyst for the discharge/charge reaction of the battery.

We have designed a hydrazine-linked COF (Figure 1) whereby the pores are rimmed by ketone oxygen and imine nitrogen atoms; these functional groups undergo coordination with Ru. Through these coordination bonds, the edges of COF are interfaced to Ru@CNT, giving rise to shorter paths to catalytic sites for CO_2 molecules and Li ions. The hydrazone COF (Tf–DHzOPr) was synthesized via condensation of benzene-1,3,5-tricarboxaldehyde (Tf) and 2,5-dipropoxytereph-thalohydrazide (DHzOPr) in the presence of an acetic acid catalyst. As confirmed by powder X-ray diffraction (PXRD) pattern, the synthesized COF exhibited good crystallinity as shown in Figure 2a, with major peaks at 3.40°, 5.93°, 6.85°, 9.17°, and
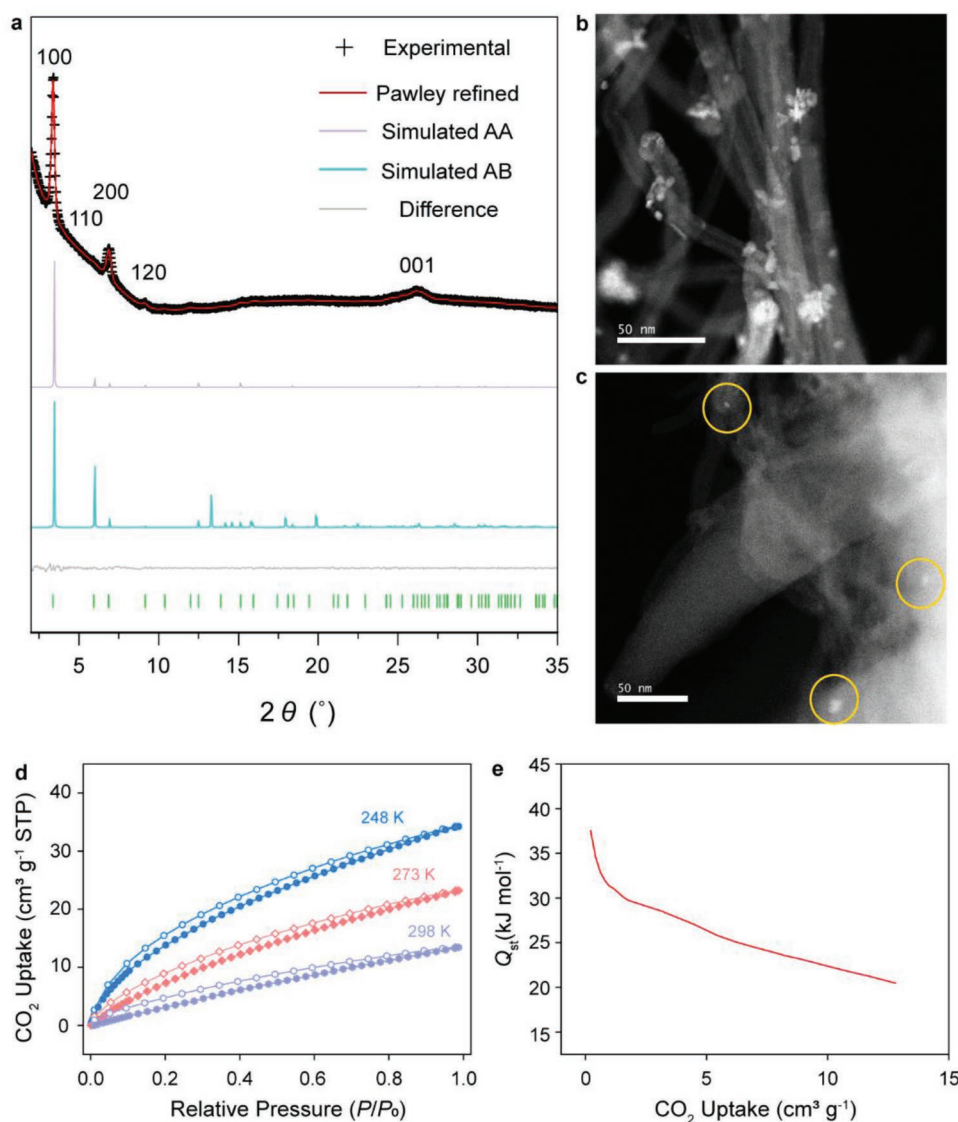
Figure 2. Characterization of Tf–DHzOPr COF and COF-Ru@CNT cathode. a) Indexed PXRD pattern of Tf–DHzOPr COF and its simulated PXRD of AA and AB stacking. b) Dark-field STEM image of Ru@CNT. c) Dark-field STEM image of COF-Ru@CNT. (Ru nanoparticles are highlighted in the yellow circles). d) CO_2 sorption isotherms of COF-Ru@CNT at 248, 273, and 298 K. e) Isosteric heat of adsorption curve of COF-Ru@CNT.

26.23°, which are assigned to (100), (110), (200), (120), and (001) facets, respectively. The Pawley refinement exhibits a good match to the experimental PXRD with $R_{wp} = 1.92\%$ and $R_p = 1.46\%$. Furthermore, the eclipsed (AA) and staggered (AB) stacked structures of Tf–DHzOPr COF were simulated (Figure 2a). The simulated PXRD reveals that the eclipsed stacking agrees better with the experimental result.

The permanent porosity of Tf–DHzOPr COF was confirmed by gas sorption experiments. Nitrogen sorption experiment at 77 K revealed a reversible type I isotherm for Tf–DHzOPr, which is characteristic of microporous materials (Figure S2, Supporting Information). The synthesized COF showed a Brunauer–Emmett–Teller (BET) surface area of 871 m^2 g^{-1}, with a total pore volume of 0.77 cm^3 g^{-1} at $P/P_0 = 0.99$. Using nonlocal density functional theory (NLDFT) calculations, a narrow pore size distribution was retrieved with a pore width

of 1.69 nm, which is consistent with the theoretical value of 1.79 nm based on the refined crystal structure. Moreover, nitrogen sorption experiment at 77 K was also conducted for COF-Ru@CNT, which showed a similar isotherm as Tf–DHzOPr (Figure S3, Supporting Information). However, the isotherm of COF-Ru@CNT displays an abrupt increase at $P/P_0 > 0.9$, which could be due to stacking defects caused by the addition of Ru@CNT. COF-Ru@CNT exhibits an estimated BET surface area of 354 m^2 g^{-1}, and a total pore volume of 0.80 cm^3 g^{-1} at $P/P_0 = 0.99$. Pore size distribution as determined by NLDFT calculation reveals a narrow pore at 1.69 nm that agrees well with the dimension of the COF channels in our materials, followed by broad peaks at large pore diameter (>10 nm). The latter indicates the presence of stacking defects in COF-Ru@CNT, which can be caused by the random stacking of CNT particles.

To test the ability of the various COF-based cathodes for CO_2 capture, CO_2 sorption experiments for Tf–DHzOPr COF and COF-Ru@CNT were conducted at 248, 273, and 298 K, respectively (Figure 2d; Figure S4, Supporting Information). The as-prepared Tf–DHzOPr COF exhibited a CO_2 uptake capacity of 65.8 cm^3 g^{-1} (1 atm, 248 K), 51.2 cm^3 g^{-1} (1 atm, 273 K), and 25.6 cm^3 g^{-1} (1 atm, 298 K). In comparison, COF-Ru@CNT displayed a CO_2 uptake capacity of 34.2 cm^3 g^{-1} (1 atm, 248 K), 23.2 cm^3 g^{-1} (1 atm, 273 K), and 13.4 cm^3 g^{-1} (1 atm, 298 K). The halved CO_2 capacity in COF-Ru@CNT is due to the incapability of Ru@CNT for CO_2 capture. However, the design of COF-Ru@CNT is to interface the COF to Ru@CNT via the hydrazide–Ru coordination at pore entrances, and thus the affinity of COF-Ru@CNT to CO_2 gas should not be affected due to the unblocked channels. The isosteric heat of adsorption (Q_{st}) curves were calculated from the CO_2 sorption isotherm at 248, 273, and 298 K to study the CO_2 affinity of the materials at different levels of CO_2 uptake (Figure 2e; Figure S4b, Supporting Information). The curve exhibited a similar Q_{st} value of 33.0 kJ mol^{-1} for Tf–DHzOPr COF and 37.5 kJ mol^{-1} for COF-Ru@CNT at low coverage. Meanwhile, the high Q_{st} value of COF-Ru@CNT indicates the strong affinity of the cathode material for CO_2 gas, which is expected to be beneficial for the sequestration of CO_2 for fast battery kinetics.

COF-Ru@CNT was synthesized by mixing highly crystalline Tf–DHzOPr COF with Ru@CNT ("Synthetic Procedure" section in the Supporting Information). The PXRD spectra (Figure S5, Supporting Information) suggest the COF-Ru@CNT composite was successfully prepared with the characteristic peaks of Ru nanoparticles at 38.3° and 43.8°.[40] Dark-field STEM showed that the COF flakes covered Ru@CNT uniformly with a high coverage, which reflects that our strategy of binding COF onto Ru@CNT via hydrazide–Ru coordination was successful (Figure 2c). The binding of the hydrazide units at the pore edges of COF to the Ru nanoparticles is verified by Fourier transform infrared (FT-IR), solid-state ^{13}C NMR, and XPS spectroscopy. FT-IR spectroscopy (Figure S6, Supporting Information) reveals a prominent intensity increase of the hydrazide C=O stretching band in COF-Ru@CNT compared to the pristine Tf–DHzOPr COF, with a significant redshift from 1672 to 1666 cm^{-1}. This is caused by the successful coordination of Ru to the hydrazide functional group, which weakens the C=O bond. In addition, a slight blueshift of the hydrazide N−H stretching band is observed for COF-Ru@CNT, indicating the Ru coordination redistributes the electron density in the hydrazide functionality. On the other hand, most IR bands are unchanged, including the fingerprint region such as the aromatic C−C stretching and C−O stretching, suggesting that the chemical integrity of the COF is intact in the COF-Ru@CNT composite. Furthermore, solid-state ^{13}C NMR study (Figure S7, Supporting Information) exhibits a downfield shift for a small portion of amide carbon and imine carbon, suggesting that the electron density at the carbon atoms is reduced by the coordination between hydrazide and Ru nanoparticles. In addition, XPS spectra of Tf–DHzOPr COF and COF-Ru@CNT revealed a different binding energy of 400.2 and 400.0 eV, respectively, for N 1s as a result of the coordination (Figure S18, Supporting Information).

Scanning electron microscopy (SEM) verified the morphology of Tf–DHzOPr COF and COF-Ru@CNT (Figures S8

and S9, Supporting Information). Tf–DHzOPr COF crystallized as nanosized spike rods that self-assembled into rod structures (Figure S8, Supporting Information). The SEM image of COF-Ru@CNT showed that CNTs were entangled with the COF (Figure S9b, Supporting Information), indicating the successful hybridization of COF and Ru@CNT via interfacial coordination.

We should clarify that the role of COF, with its ordered 1D channel, is mainly as the CO_2 gas/Li ion transport channels in the Li–CO_2 cathode, whereas Ru(0) nanoparticles act as the catalyst for battery discharge/charge. To understand the role of COF in the electrode, battery performance of pristine CNT, COF-CNT (1:1 weight ratio mixture of Tf–DHzOPr and CNT), Ru@CNT, and COF-Ru@CNT was compared. The specific capacity of the Li–CO_2 batteries was determined by the full discharge/charge curves at a current density of 200 mA g^{-1} (**Figure 3**a). The active materials for specific capacity calculation are CNT, COF-CNT, Ru@CNT, and COF-Ru@CNT for each cathodes (see the "Electrochemical Measurements" section in the Supporting Information). The specific capacities of batteries with CNT, COF-CNT, Ru@CNT, and COF-Ru@CNT cathodes are 9045, 25 163, 9836, and 27 348 mAh g^{-1} (2.44, 6.79, 2.65, and 7.38 mAh cm^{-2}), respectively. The cathodes with COF exhibit very high capacities, which exceed those without COF by a wide margin. This suggests that the open channel network in crystalline COF boasts the CO_2 intake of the electrode, and the high specific surface area of COF aids in the formation of discharge products (Li_2CO_3/C), which gives rise to the excellent specific capacity. In addition, COF-Ru@CNT cathode discharges 93% of the capacity above 2.4 V, indicating the application prospect of Li–CO_2 batteries with the COF-based cathodes in high-energy power supply. As far as we know, COF-Ru@CNT possesses the highest specific capacity among all reported Li–CO_2 batteries. Upon recharge, COF-Ru@CNT cathode is able to be fully recharged to 27 348 mAh g^{-1} (100% recharge) under 4.27 V, meaning discharge products can be completely decomposed under low charge voltage. On the other hand, Ru@CNT cathode can be only recharged to a capacity of 9308 mAh g^{-1} (94.6% of 9836 mAh g^{-1}) with a high cutoff voltage of 4.5 V. The results indicate that the presence of COF helps with Li_2CO_3/C decomposition. Although our hydrazide/hydrazone COF (Tf–DHzOPr) is not the best-performing material for gas-phase CO_2 capture, we rationalize its excellent specific capacity based on its ability to act as both ion transport channel and solid-state electrolyte for capturing CO_2. The CO_2 capture process is different in Li–CO_2 battery because the cathode needs to intake the CO_2 molecules from electrolyte solution. Through coordination of the hydrazone COF to Ru@CNT, COF provides diffusion channels on the cathode, whereby CO_2 gas and Li^+ ions travel a shorter path to the catalytic sites. In contrast, the diffusion pathways are quickly clogged by discharge products in cathodes without COFs, leading to poor capacities.

It is known that severe polarization in Li–CO_2 battery gives rise to large charge/discharge overpotential. This is not only because of the high energy barrier for Li_2CO_3 decomposition, but also caused by poor electrode kinetics due to the sluggish diffusion of reactants (such as CO_2 and Li ions). When COFs are immobilized onto the battery catalyst and current collectors, both CO_2 and Li ions can be channeled to catalytic sites of
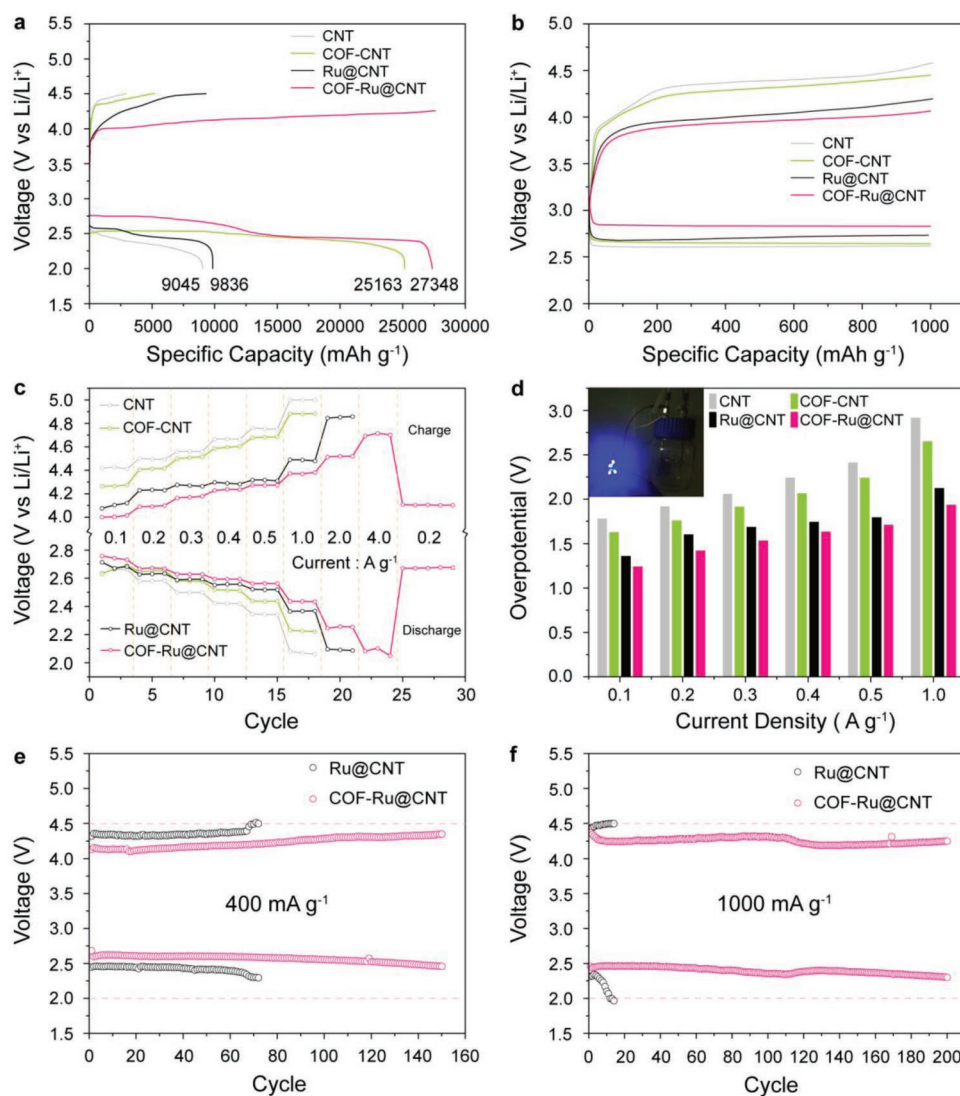
Figure 3. The electrochemical performances of Li–CO$_2$ batteries with CNT, COF-CNT, Ru@CNT, and COF-Ru@CNT cathodes. a) Full discharge curves at a current density of 200 mA g^{-1}. b) The first discharge/charge profiles within a limiting capacity of 1000 mAh g^{-1} at a current density of 200 mA g^{-1}. c) Rate performances within a limiting capacity of 1000 mAh g^{-1} at various current densities. d) Battery overpotentials at various current densities (inset: four blue LEDs in parallel were lighted brightly by the Li–CO$_2$ battery with COF-Ru@CNT cathode). e,f) Battery life cycles of Ru@CNT cathode and COF-Ru@CNT cathode at a current density of 400 mA g^{-1} (e) and 1000 mA g^{-1} (f).

Ru nanoparticles, greatly facilitating the kinetics during battery discharge/charge. Strong evidence for this comes from comparing the battery overpotentials of CNT, COF-CNT, Ru@CNT, and COF-Ru@CNT cathodes. The overpotentials of batteries were determined by the differences of the cutoff charge and discharge potentials at a current density of 200 mA g^{-1} within a limiting capacity of 1000 mAh g^{-1} (Figure 3b). Without the Ru catalyst, CNT cathode displays a charge potential of 4.58 V and a discharge potential of 2.61 V, whereas COF–CNT cathode displays a charge potential of 4.45 V and a discharge potential of 2.64 V. Even in the absence of Ru catalyst, the decrease of overpotential in COF-based cathode clearly suggests that the enhanced kinetics promoted by the 1D channels of COF alone can mitigate the severe polarization issue in Li–CO$_2$ batteries to some extent. Moreover, the battery with COF–CNT can be charged

under 4.5 V for cycling, illustrating the stability of the COF channels (Figure S12b, Supporting Information). Upon the immobilization of Ru catalysts, Ru@CNT exhibits a charge potential of 4.20 V and a discharge potential of 2.73 V, which is comparable with a reported Ru nanoparticle-decorated Super P cathode (a charge potential of 4.25 V and a discharge potential of 2.54 V).[40] Furthermore, COF-Ru@CNT exhibits the lowest charge potential of 4.07 V and the highest discharge potential of 2.83 V among the four cathodes. The four cathodes show overpotentials of 1.97, 1.81, 1.47, and 1.24 V for CNT, COF-CNT, Ru@CNT, and COF-Ru@CNT, respectively. At 200 mA g^{-1} and within capacity of 1 Ah g^{-1}, the overpotential exhibits negligible decay during battery cycling of COF-Ru@CNT, suggesting the good stability of the cathode (Figure S12d, Supporting Information). The reduced overpotential indicates that COF diffusion

**ADVANCED
SCIENCE NEWS**
www.advancedsciencenews.com

**ADVANCED
MATERIALS**
www.advmat.de

channels and Ru catalyst work synergistically to alleviate the polarization in battery charge/discharge.

To further understand how COF helps ion diffusion and improve battery kinetics, electrochemical impedance spectroscopy (EIS) of Ru@CNT and COF-Ru@CNT cathodes was measured (Figure S13, Supporting Information). The Nyquist plots exhibit linear increase at low frequency, which is characteristic of mass diffusion-controlled process for Li ion. Noticeably, the Nyquist plot of COF-Ru@CNT cathode shows a much larger gradient, indicating a lower diffusion impedance compared to Ru@CNT cathode. Based on the Nyquist plots and Equation S2 (Supporting Information), the Li-ion diffusion coefficients' ratio of COF-Ru@CNT and Ru@CNT is determined to be 11:1, implying a much better kinetics in COF-Ru@CNT cathode for Li-ion transport. Through electrical resistance measurement, we also confirmed the electrical conductance in COF-Ru@CNT cathode was not affected by the presence of COF. COF-Ru@CNT powder and CNT were pressed into pellets separately. Due to uniform coupling of COF and CNTs via Ru coordination, the in-plane resistance of COF-Ru@CNT pellet showed negligible decrease compared to that of CNT pellet (Figure S14, Supporting Information). In addition, the internal resistances of batteries using Ru@CNT or COF-Ru@CNT cathode as measured by EIS analysis show negligible difference, with values of 7.9 and 8.5 Ω, respectively (Figure S15, Supporting Information). These results suggest that the hybridization of COF and Ru@CNT through interface coordination can efficiently enhance the ion diffusion and kinetics in batteries.

One positive outcome brought by the enhanced battery kinetics is the remarkable improvement of rate performance. Due to sluggish kinetics of the discharging and charging reactions, Li–CO$_2$ batteries invariably display disastrously poor rate performance. Here, we thoroughly compared the rate performance of batteries with the four different cathodes of CNT, COF-CNT, Ru@CNT, and COF-Ru@CNT. The rate performance was evaluated by the end discharging/charging voltage of the batteries at various current densities within a limiting capacity of 1000 mAh g^{-1} (Figure 3c). Without Ru catalyst, the cathodes generally show poor rate with a dramatic decrease of discharging voltage and increase of charging voltage when the current density is increased from 0.1 to 1 A g^{-1}. However, COF–CNT cathode exhibits a better rate performance with a smaller discharge potential loss (≈2.65–2.22 V) and a charge potential increase (≈4.26–4.88 V), whereas pure CNT cathode shows a discharge potential decay (≈2.65–2.07 V) and charge potential rise (≈4.42 V to the upper limit voltage of 5 V) when current density varies from 0.1 to 1 A g^{-1}. This evidence indicates that even in the absence of Ru catalyst, COF can improve the kinetics in Li–CO$_2$ battery. In the presence of Ru catalyst, Ru@CNT cathode exhibits a much better rate at small current density (<1 A g^{-1}), with discharging voltage loss (≈2.71–2.37 V) and charging voltage increase (≈4.10–4.48 V). Nevertheless, when the current density increases to 2 A g^{-1}, the discharging voltage of Ru@CNT cathode dramatically drops below 2.1 V, while the charging voltage rises sharply to ≈4.85 V. To our delight, the battery using COF-Ru@CNT cathode displays the best rate with a slow decay of discharging voltage from ≈2.75 to ≈2.44 V and a slow increase of charging voltage

from ≈4.00 to ≈4.37 V when the current density is increased to 1000 mA g^{-1}; the battery even survives an ultrahigh current density of 4000 mA g^{-1} and exhibits no loss of discharging voltage when the current density returned to 200 mA g^{-1}. The battery overpotentials for the four cathodes at various rates are summarized in Figure 3d. Furthermore, four blue light-emitting diode (LED) bulbs connected in parallel can be lighted brightly using our COF-Ru@CNT battery, suggesting its excellent rate performance (Figure 3d, inset). These results suggest that our COF-based Li–CO$_2$ batteries are potential candidates for energy storage devices with high capacity and good rate performance.

The above results show that the cooperation between COF 1D channels and Ru catalyst efficiently narrows down the overpotential and enhances the battery kinetics, allowing the battery to run longer cycles and endure higher current densities. We first examined the battery cycling performance of Ru@CNT and COF-Ru@CNT at a relatively low current density of 0.4 A g^{-1}. The battery with Ru@CNT cathode runs for 70 cycles at this current density, which is comparable to previously reported Li–CO$_2$ battery with Ru@Super P cathode.[40] In contrast, COF-Ru@CNT battery runs for 150 cycles with a smaller overpotential and shows no obvious decay of battery performance (Figure 3e).

To test performance under higher-stress cycles, we tested the battery cycle life under a high current density of 1000 mA g^{-1} (Figure 3f). The battery with COF-Ru@CNT cathode runs for 200 cycles with no obvious performance decay within a limiting capacity of 1000 mAh g^{-1}. When the limiting capacity (1000 mAh g^{-1}) is increased to 3000 mAh g^{-1} at 200 mA g^{-1}, the cells perform with high stability up to 30 cycles (Figure S16, Supporting Information). Under a high current density of 1000 mA g^{-1} and a high limiting capacity of 3000 mAh g^{-1}, the battery still cycles efficiently with negligible decay of discharge/charge potentials. On the other hand, batteries with Ru@CNT cathode can only run 14 cycles at the current density of 1000 mA g^{-1}.

The poor stability of Li–CO$_2$ batteries is mainly caused by the incomplete decomposition of Li$_2$CO$_3$ during the charging process; the residues build up and passivate the cathode surface, clog diffusion channels, and degrade battery performance. We observed that the presence of COF ion/gas diffusion channels on the cathode prevents Li$_2$CO$_3$ accumulation. First, we confirmed stability of the COF-based cathode. The cyclic voltammetry (CV) of the battery with COF-Ru@CNT cathode suggests that COF did not participate in the redox reactions in the electrochemical window of 2.0–4.5 V (Figure S10, Supporting Information). In addition, we have also confirmed that the crystallinity of the COF in COF-Ru@CNT cathode is maintained after multiple CV cycles (2.0–4.3 V) via PXRD study (Figure S17, Supporting Information). Ex situ SEM was used to trace Li$_2$CO$_3$ in the cathodes after discharge and charge within a limited capacity of 1000 mAh g^{-1}. After discharge, both Ru@CNT and COF-Ru@CNT cathodes were covered with plate-like nanoparticles of Li$_2$CO$_3$ (**Figure 4**; Figures S21 and S22, Supporting Information). There are significantly less Li$_2$CO$_3$ aggregates detected on COF-Ru@CNT after ten cycles of discharge/charge as compared to Ru@CNT cathode, where Li$_2$CO$_3$ agglomerates could be observed after the first discharge/charge cycle (Figure 4f). According to ex situ X-ray diffraction (XRD) spectra (Figure 4i,j), new peaks at 21.2°, 30.5°, and 31.6°, corresponding
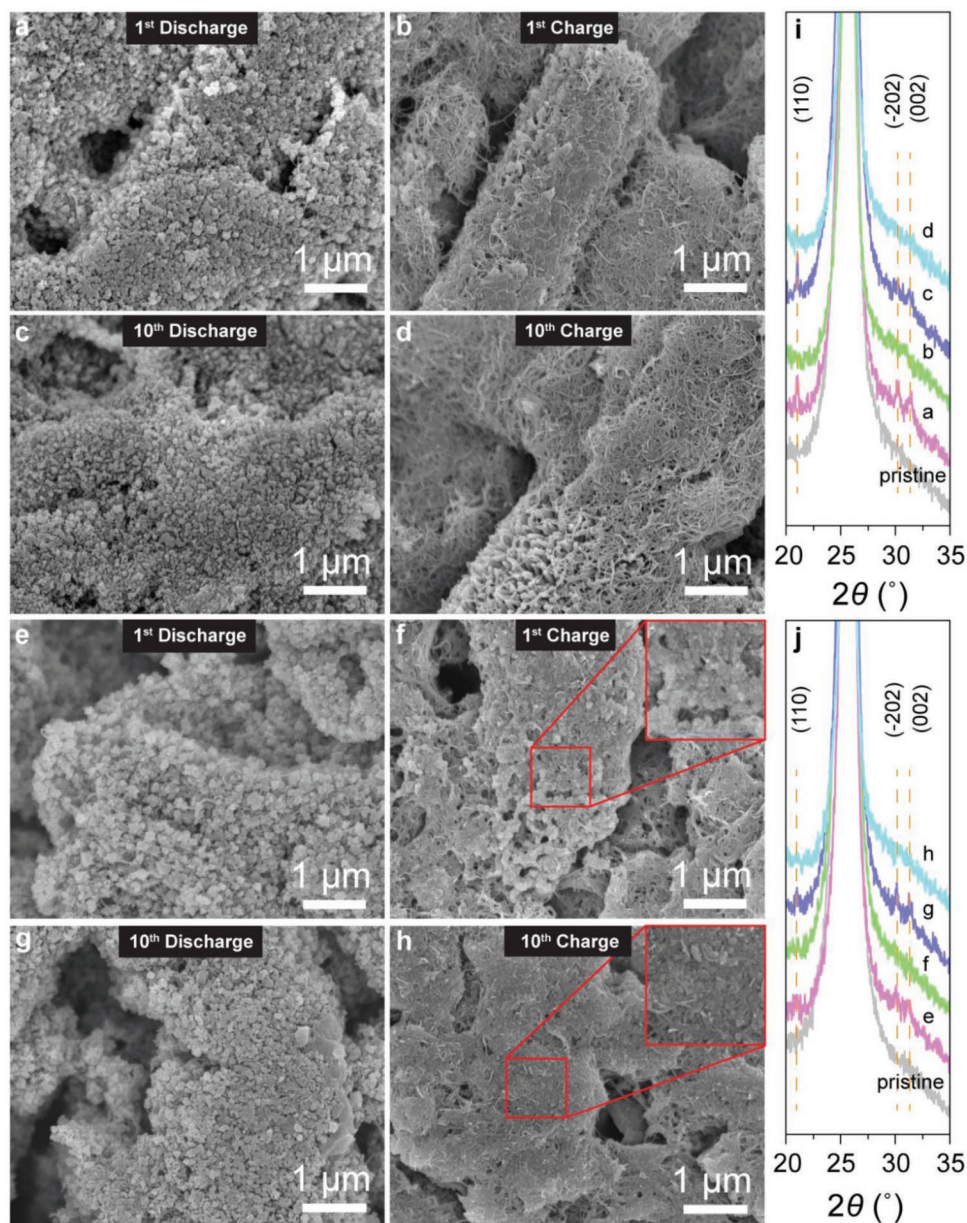
Figure 4. Tracing of Li_2CO_3 in the cathodes after discharge and charge processes at a current of 200 mA g^{-1} and a limited capacity of 1000 mAh g^{-1}. a–d) The SEM images of COF-Ru@CNT cathodes after first discharge (a), first charge (b), tenth discharge (c), and tenth charge (d), and e–h) Ru@CNT cathodes after first discharge (e), first charge (f), tenth discharge (g), and tenth charge (h). i,j) PXRD of COF-Ru@CNT cathodes (i) and Ru@CNT cathodes (j) after different discharge/charge processes.

to (110), (–202), and (202) planes of Li_2CO_3 crystals (PDF #22-1411), respectively, are present after discharging process in both Ru@CNT cathode and COF-Ru@CNT cathodes. This suggests that crystalline Li_2CO_3 was the main discharge product of the batteries. To assess the reversibility of the discharge/charge cycles, XPS was used to monitor the presence or absence of discharged product in Ru@CNT and COF-Ru@CNT cathodes after multiple battery cycles (**Figure 5**; Figure S19, Supporting Information). Both Ru@CNT and COF-Ru@CNT cathodes show the appearance of the Li_2CO_3 peak at 290.2 eV after discharge. Importantly, it was observed that Ru@CNT cathode exhibits Li_2CO_3 accumulation after ten cycles of discharging/charging,

whereas COF-Ru@CNT cathode reveals only a trace amount of Li_2CO_3 after ten cycles. Therefore, the presence of COF facilitates the efficient decomposition of discharge product, which is critical for improving the charging reactions in Li–CO$_2$ batteries. Since COF is insulating, redox reactions do not occur within the channels; although it can facilitate fast ion and gas transport, this ensures that the channel is not clogged up by reduction products. In return, these unblocked channels help with the sequestration of CO_2 and its transport during discharging and charging processes, thereby alleviating Li_2CO_3 accumulation.

In conclusion, we have developed effective ion/gas diffusion channels for cathode materials in Li–CO$_2$ batteries using
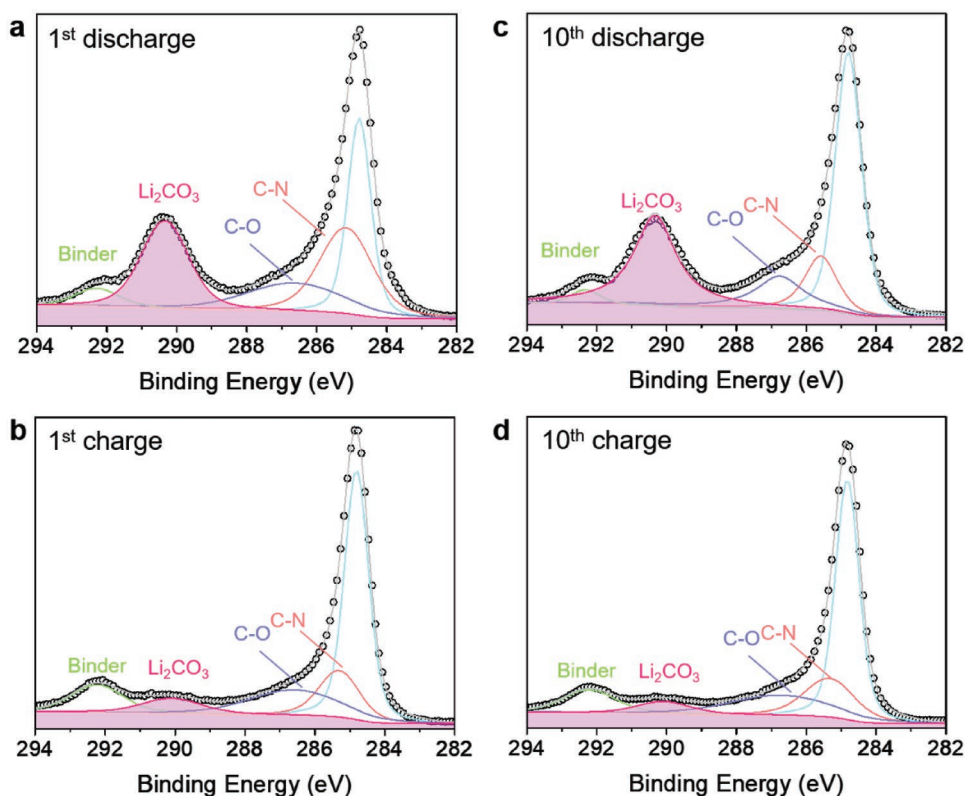
Figure 5. a–d) XPS spectra of battery cycling with COF-Ru@CNT cathodes after first discharge (a), first charge (b), tenth discharge (c), and tenth charge (d).

a hydrazone/hydrazide-containing COF. This allows us to achieve improved capacity, overpotential, stability, and rate performance in Li–CO_2 batteries. The excellent performance is attributed to the well-tailored 1D channels and functionalities in COF that allow both CO_2 capture and diffusion as well as fast Li-ion transport; these synergistic effects promote the rapid formation/decomposition of Li_2CO_3 during the discharge/charge process. The favorable properties of COF for simultaneous gas and ion transport should not only be limited only to Li–CO_2 batteries, but also applicable to a wide range of metal–air batteries. The use of COF as gas/ion diffusion channels may pave the way toward realizing the full potential of metal–gas batteries.

Supporting Information

Supporting Information is available from the Wiley Online Library or from the author.

Acknowledgements

Conflict of Interest

The authors declare no conflict of interest.

Keywords

[1] P. J. Waller, F. Gándara, O. M. Yaghi, *Acc. Chem. Res.* **2015**, *48*, 3053.

[2] N. Huang, P. Wang, D. Jiang, *Nat. Rev. Mater.* **2016**, *1*, 16068.

[3] C. S. Diercks, O. M. Yaghi, *Science* **2017**, *355*, eaal1585.

[4] S. Kandambeth, K. Dey, R. Banerjee, *J. Am. Chem. Soc.* **2019**, *141*, 1807.

[5] X. Li, Q. Gao, J. Wang, Y. Chen, Z.-H. Chen, H.-S. Xu, W. Tang, K. Leng, G.-H. Ning, J. Wu, Q.-H. Xu, S. Y. Quek, Y. Lu, K. P. Loh, *Nat. Commun.* **2018**, *9*, 2335.

[6] E. Jin, J. Li, K. Geng, Q. Jiang, H. Xu, Q. Xu, D. Jiang, *Nat. Commun.* **2018**, *9*, 4143.

[7] S. Lin, C. S. Diercks, Y.-B. Zhang, N. Kornienko, E. M. Nichols, Y. Zhao, A. R. Paris, D. Kim, P. Yang, O. M. Yaghi, C. J. Chang, *Science* **2015**, *349*, 1208.

[8] V. S. Vyas, F. Haase, L. Stegbauer, G. Savasci, F. Podjaski, C. Ochsenfeld, B. V. Lotsch, *Nat. Commun.* **2015**, *6*, 8508.

[9] P.-F. Wei, M.-Z. Qi, Z.-P. Wang, S.-Y. Ding, W. Yu, Q. Liu, L.-K. Wang, H.-Z. Wang, W.-K. An, W. Wang, *J. Am. Chem. Soc.* **2018**, *140*, 4623.

[10] S. Yang, W. Hu, X. Zhang, P. He, B. Pattengale, C. Liu, M. Cendejas, I. Hermans, X. Zhang, J. Zhang, J. Huang, *J. Am. Chem. Soc.* **2018**, *140*, 14614.

[11] C. R. DeBlase, K. E. Silberstein, T.-T. Truong, H. D. Abruña, W. R. Dichtel, *J. Am. Chem. Soc.* **2013**, *135*, 16821.

[12] F. Xu, S. Jin, H. Zhong, D. Wu, X. Yang, X. Chen, H. Wei, R. Fu, D. Jiang, *Sci. Rep.* **2015**, *5*, 8225.

[13] S. Wang, Q. Wang, P. Shao, Y. Han, X. Gao, L. Ma, S. Yuan, X. Ma, J. Zhou, X. Feng, B. Wang, *J. Am. Chem. Soc.* **2017**, *139*, 4258.

[14] A. Halder, M. Ghosh, A. Khayum M, S. Bera, M. Addicoat, H. S. Sasmal, S. Karak, S. Kurungot, R. Banerjee, *J. Am. Chem. Soc.* **2018**, *140*, 10941.

[15] K. Sumida, D. L. Rogow, J. A. Mason, T. M. McDonald, E. D. Bloch, Z. R. Herm, T.-H. Bae, J. R. Long, *Chem. Rev.* **2012**, *112*, 724.

[16] Y. Zeng, R. Zou, Y. Zhao, *Adv. Mater.* **2016**, *28*, 2855.

[17] H. Furukawa, O. M. Yaghi, *J. Am. Chem. Soc.* **2009**, *131*, 8875.

[18] C. J. Doonan, D. J. Tranchemontagne, T. G. Glover, J. R. Hunt, O. M. Yaghi, *Nat. Chem.* **2010**, *2*, 235.

[19] N. Huang, X. Chen, R. Krishna, D. Jiang, *Angew. Chem., Int. Ed.* **2015**, *54*, 2986.

[20] N. Huang, R. Krishna, D. Jiang, *J. Am. Chem. Soc.* **2015**, *137*, 7079.

[21] Z. Kang, Y. Peng, Y. Qian, D. Yuan, M. A. Addicoat, T. Heine, Z. Hu, L. Tee, Z. Guo, D. Zhao, *Chem. Mater.* **2016**, *28*, 1277.

[22] Q. Gao, X. Li, G.-H. Ning, H.-S. Xu, C. Liu, B. Tian, W. Tang, K. P. Loh, *Chem. Mater.* **2018**, *30*, 1762.

[23] S. Chandra, T. Kundu, S. Kandambeth, R. BabaRao, Y. Marathe, S. M. Kunjir, R. Banerjee, *J. Am. Chem. Soc.* **2014**, *136*, 6570.

[24] H. Xu, S. Tao, D. Jiang, *Nat. Mater.* **2016**, *15*, 722.

[25] C. Montoro, D. Rodríguez-San-Miguel, E. Polo, R. Escudero-Cid, M. L. Ruiz-González, J. A. R. Navarro, P. Ocón, F. Zamora, *J. Am. Chem. Soc.* **2017**, *139*, 10079.

[26] Y. Du, H. Yang, J. M. Whiteley, S. Wan, Y. Jin, S.-H. Lee, W. Zhang, *Angew. Chem., Int. Ed.* **2016**, *55*, 1737.

[27] Y. Zhang, J. Duan, D. Ma, P. Li, S. Li, H. Li, J. Zhou, X. Ma, X. Feng, B. Wang, *Angew. Chem., Int. Ed.* **2017**, *56*, 16313.

[28] Q. Xu, S. Tao, Q. Jiang, D. Jiang, *J. Am. Chem. Soc.* **2018**, *140*, 7429.

[29] G. Zhang, Y.-l. Hong, Y. Nishiyama, S. Bai, S. Kitagawa, S. Horike, *J. Am. Chem. Soc.* **2019**, *141*, 1227.

[30] Z. Guo, Y. Zhang, Y. Dong, J. Li, S. Li, P. Shao, X. Feng, B. Wang, *J. Am. Chem. Soc.* **2019**, *141*, 1923.

[31] S. Xu, S. K. Das, L. A. Archer, *RSC Adv.* **2013**, *3*, 6656.

[32] Z. Zhang, Q. Zhang, Y. Chen, J. Bao, X. Zhou, Z. Xie, J. Wei, Z. Zhou, *Angew. Chem., Int. Ed.* **2015**, *54*, 6550.

[33] X. Zhang, Q. Zhang, Z. Zhang, Y. Chen, Z. Xie, J. Wei, Z. Zhou, *Chem. Commun.* **2015**, *51*, 14636.

[34] Z. Xie, X. Zhang, Z. Zhang, Z. Zhou, *Adv. Mater.* **2017**, *29*, 1605891.

[35] Y. Qiao, J. Yi, S. Wu, Y. Liu, S. Yang, P. He, H. Zhou, *Joule* **2017**, *1*, 359.

[36] S. Li, Y. Dong, J. Zhou, Y. Liu, J. Wang, X. Gao, Y. Han, P. Qi, B. Wang, *Energy Environ. Sci.* **2018**, *11*, 1318.

[37] Y. Qiao, Y. Liu, C. Chen, H. Xie, Y. Yao, S. He, W. Ping, B. Liu, L. Hu, *Adv. Funct. Mater.* **2018**, *28*, 1805899.

[38] S. Xu, C. Chen, Y. Kuang, J. Song, W. Gan, B. Liu, E. M. Hitz, J. W. Connell, Y. Lin, L. Hu, *Energy Environ. Sci.* **2018**, *11*, 3231.

[39] D. R. Williams, National Space Science Data Center, NASA https://nssdc.gsfc.nasa.gov/planetary/factsheet/marsfact.html (accessed: October 2019).

[40] S. Yang, Y. Qiao, P. He, Y. Liu, Z. Cheng, J.-j. Zhu, H. Zhou, *Energy Environ. Sci.* **2017**, *10*, 972.

[41] Y. Hou, J. Wang, L. Liu, Y. Liu, S. Chou, D. Shi, H. Liu, Y. Wu, W. Zhang, J. Chen, *Adv. Funct. Mater.* **2017**, *27*, 1700564.

[42] S. Bie, M. Du, W. He, H. Zhang, Z. Yu, J. Liu, M. Liu, W. Yan, L. Zhou, Z. Zou, *ACS Appl. Mater. Interfaces* **2019**, *11*, 5146.

[43] X. Zhang, C. Wang, H. Li, X.-G. Wang, Y.-N. Chen, Z. Xie, Z. Zhou, *J. Mater. Chem. A* **2018**, *6*, 2792.

[44] C. Wang, Q. Zhang, X. Zhang, X.-G. Wang, Z. Xie, Z. Zhou, *Small* **2018**, *14*, 1800641.

[45] G.-H. An, H. An, H.-J. Ahn, *J. Electroanal. Chem.* **2016**, *775*, 280.